

Finite Element and Machine Learning Modeling of Autogenous Self-Healing Concrete

William Liu^{1,2}

²Pennsylvania State University, University Park, Pennsylvania, USA 16802.
liuwilliam12@gmail.com

October 24, 2025

Abstract

A time-dependent modeling framework for autogenous self-healing concrete that couples moisture diffusion with damage evolution was developed. Water transport follows Fick’s second law with a damage-dependent diffusivity obtained by power-law interpolation between intact concrete and crack space. Healing reduces damage in proportion to local moisture and a smoothed cement availability field computed via a Helmholtz filter. Two finite element variants were implemented in FEniCSx over time horizons up to 5×10^6 seconds: a Crack Diffusion Model (CDM) with standard diffusion and a Crack Membrane Model (CMM) that gates cross-crack transport until a critical moisture threshold is reached. Key control parameters are the initial crack orientation and size, the diffusion coefficients of intact and cracked concrete, the healing rate constant, and the cement availability smoothing parameter. Simulations on a unit square domain show that healing time varies non-monotonically with crack orientation, peaking near 45° and 135° and minimizing near 90° , consistent with diffusion distance to crack endpoints dominating the process. The dependence on crack width reverses with material parameters: healing time increases when $D_{\text{cracked}} < D_{\text{intact}}$ and decreases when $D_{\text{cracked}} > D_{\text{intact}}$. The CMM reproduces staged moisture penetration with delayed gate activation but lengthens total healing time, whereas the CDM is efficient for parametric sweeps. Machine learning classifiers trained on one million simulation samples predict binary healing outcomes $H(\sigma, \gamma, t)$ (healed or not) with high accuracy (up to 0.998 for neural networks). Although experimental calibration is still required, the framework provides a versatile tool for guiding laboratory studies and implementations of self-healing concrete.

1 Introduction

Concrete is the second most widely used material globally, surpassed only by water, with over 30 billion metric tons utilized worldwide annually [1]. This critical construction material has been employed for over 8,000 years, dating back to concrete-like structures built by Nabataea traders in modern-day Syria [2], and continues to be essential for housing, transportation, and water infrastructure today. The global concrete market is projected to reach \$821.6 billion by 2026 [3], driven by growing investment in construction projects worldwide.

However, concrete production and usage come with significant environmental and economic costs. The concrete industry contributes approximately 8% of global CO₂ emissions, exceeding the combined emissions from the aviation (3.5%) and shipping (3%) industries [4]. Under current trajectories, carbon emissions from concrete production are expected to increase from 1.6 billion tonnes today to 3.8 billion tonnes annually by 2050 [5]. To meet the Paris Climate Agreement’s 1.5°C warming limit, the global concrete industry must reduce emissions by 16% by 2030 and achieve

net-zero emissions by 2050, while simultaneously addressing the projected 48% increase in cement demand from 4.2 billion to 6.2 billion tons by 2050 [6].

The infrastructure crisis compounds these environmental challenges. Most countries completed their major infrastructure projects during the late 1900s, including the US Interstate Highway System, European motorways, Japan’s Shinkansen, and China’s expressway networks. Over half a century later, these aging structures face increasing failure risks, with concrete failure probability approaching 70% after 50 years and becoming nearly inevitable by the century’s end [7]. Currently, over 20,000 concrete bridges in the United States are classified as structurally deficient [8], requiring frequent maintenance and posing safety risks. The global cost of corrosion in reinforced concrete infrastructure is estimated at \$2.5 trillion annually, representing approximately 3.4% of global GDP [9].

Self-healing concrete emerges as a promising solution to address these challenges. This innovative material repairs its cracks automatically without human intervention, typically through chemical or biological processes [10]. Self-healing concrete offers reduced maintenance requirements over infrastructure lifetime, diminished social costs of reconstruction, increased infrastructure efficiency, decreased economic costs of frequent repairs, and reduced environmental impacts of regular restorations [11].

Self-healing concrete approaches are broadly categorized into two types: autogenous healing, where water penetration triggers intrinsic chemical healing reactions, and autonomous healing, which relies on discrete self-healing mechanisms added during production [10]. While autonomous healing can address larger cracks (0.1-1.8 mm), it faces challenges including low survivability during mixing, harsh biological environments, and high cost [12, 13].

For these reasons, this study focuses on autogenous self-healing concrete, which more closely resembles traditional concrete and warrants investigation for real-world implementation. Autogenous healing concrete exhibits computational tractability compared to bacteria-based concrete due to its uniformity and predictability. All concrete types possess inherent autogenous self-healing abilities through continued hydration, carbonation, and calcium silicate hydrate (C-S-H) swelling. For this study, we define autogenous self-healing concrete as a cementitious mixture specifically modified to enhance self-healing capacity.

Despite comprehensive laboratory investigations, limited real-world applications of autogenous self-healing concrete exist. The Cardiff-led Materials For Life (M4L) project conducted field trials testing six different concrete walls in Wales [14]. However, to the best of our knowledge, no dedicated implementation of autogenous self-healing concrete in civilian infrastructure has been documented.

Traditional laboratory studies typically focus on isolated environmental stressors, neglecting the compounded effects of multiple simultaneous stressors. Computer simulations offer a solution by providing cheaper, faster, and more consistent results than laboratory studies. Simulation enables modeling of multiple factors simultaneously, while laboratory equipment constraints often limit studies to only one or two stressors. Furthermore, large-scale infrastructure trials are rare and expensive, making simulation models valuable precursors to further investment.

Previous research has established a foundation for finite element analysis and physics-based modeling of autogenous self-healing concrete [15, 16, 17, 18]. However, several limitations persist across existing studies: (1) isotropic diffusion and healing assumptions that neglect anisotropic variations in concrete crystal matrices, (2) neglect of time-dependence and feedback mechanisms at each time step, (3) lack of experimental calibration or validation, and (4) simplified 2D domains that may not capture complex three-dimensional healing processes.

This paper presents a coupled simulation model that integrates multiple relevant physical and chemical processes previously overlooked. We developed two distinct model versions using the FEniCSx finite element software [19]: the Crack Diffusion Model (CDM) implementing standard

diffusion across crack interfaces, and the Crack Membrane Model (CMM) implementing a binary gate that selectively allows diffusion only after reaching critical moisture levels. The models incorporate time-dependent feedback mechanisms, realistic diffusion coefficients, and damage evolution relating cement and water availability.

The remainder of this paper is organized as follows: Section 2 details the development of the Crack Diffusion Model, including governing equations, variables, and implementation methodology. Section 2.2 introduces the Crack Membrane Model as an enhanced approach. Section 2.3 demonstrates machine learning applications for predicting healing behavior and reducing computational costs. Section 3 presents results and analysis of healing time relationships with crack angle and width parameters, including performance comparisons between CDM and CMM models and machine learning model evaluations. Section 3.6 discusses limitations and future extensions, and Section 4 concludes with key findings and implications for infrastructure sustainability.

2 Modeling Approach

2.1 Crack Diffusion Model

CDM simulates autogenous healing through moisture transport and cement hydration processes. The model couples moisture diffusion with damage evolution, accounting for the spatial heterogeneity of concrete microstructure and the availability of unhydrated cement clinker.

Water diffusion follows Fick’s second law with a damage-dependent diffusivity:

$$\frac{\partial U}{\partial t} = \nabla \cdot (D(d)\nabla U) \quad (1)$$

where U is the water concentration variable (dimensionless), D is the diffusion coefficient ($\frac{m^2}{s}$), and d is the damage variable (dimensionless). The damage variable represents the fraction of damaged area, where $d = 0$ corresponds to intact concrete and $d = 1$ to complete damage.

The effective diffusion coefficient interpolates between intact concrete (D_{intact}) and crack space (D_{cracked}) using a power-law relationship:

$$D(d) = D_{\text{intact}}^{(1-d)^p} \cdot D_{\text{cracked}}^{(1-(1-d)^p)} \quad (2)$$

where p controls the sharpness of the transition. The crack-space diffusivity accounts for microcrack bridging, capillary effects, and tortuous percolation pathways.

Healing reduces damage through cement hydration, which is modeled as:

$$\frac{\partial d}{\partial t} = -\alpha U \cdot \chi_{\text{eff}}(d, q) \quad (3)$$

where α is the healing rate constant and χ_{eff} represents effective cement availability. The local cement availability follows:

$$\chi(d, q) = (1 - d)^q \quad (4)$$

where q controls the nonlinear decrease in cement availability with damage.

A complete crack introduces a discontinuity in the cement availability field. To enable healing modeling in completely damaged regions ($d = 1$), this discontinuity must be smoothed using Helmholtz filtering:

$$\begin{aligned} \chi_{\text{eff}}(x) - \gamma \Delta \chi_{\text{eff}}(x) &= \chi(x), \quad \forall x \in \Omega \\ \nabla \chi_{\text{eff}} \cdot n &= 0, \quad \forall x \in \partial\Omega \end{aligned} \quad (5)$$

where γ is the characteristic smoothing length scale. The spatial domain and its boundary are denoted as Ω and $\partial\Omega$, respectively.

The CDM solves the coupled system of equations introduced above using the finite element method implemented in FEniCSx, with the workflow shown in Figure 1. The time-dependent solution accounts for feedback between moisture transport, damage evolution, and cement availability.

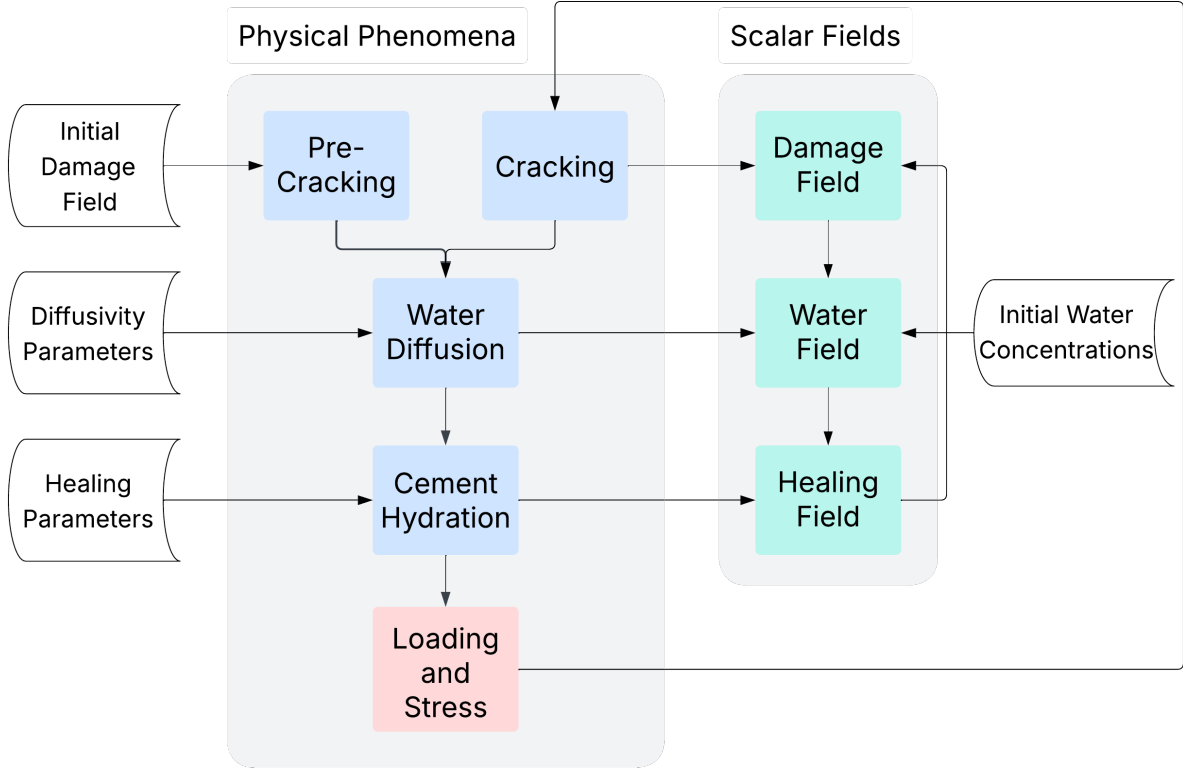


Fig. 1. Autogenous Self-Healing Concrete Simulation Workflow using CDM with Parameters, Phenomena, and Scalar Fields

2.2 Crack Membrane Model

CMM addresses a key limitation of CDM: the instantaneous water transport across cracks. In reality, water encounters resistance at crack boundaries and requires sufficient pressure to penetrate crack spaces. The CMM implements a threshold-based gating mechanism that controls water flow across damaged regions.

Specifically, CMM introduces a damage threshold $d_{\text{threshold}}$ that distinguishes intact regions ($d \leq d_{\text{threshold}}$) from cracked regions ($d > d_{\text{threshold}}$). Water transport in cracked regions is governed by a gating function $G(U)$ that depends on local moisture concentration:

$$G(U) = \epsilon_{\text{gate}} + \frac{1 - \epsilon_{\text{gate}}}{1 + \exp(-(U - U_{\text{critical}})/\Delta U_{\text{gate}})} \quad (6)$$

where U_{critical} is the critical moisture threshold, ΔU_{gate} controls the transition sharpness, and ϵ_{gate} is a small positive constant that prevents numerical instabilities.

In CMM, the effective diffusion coefficient D_{eff} becomes a function of both damage and moisture concentration:

$$D_{\text{eff}}(d, U) = \begin{cases} D(d) & \text{if } d \leq d_{\text{threshold}} \\ G(U) \cdot D(d) & \text{if } d > d_{\text{threshold}} \end{cases} \quad (7)$$

This formulation suppresses water flow in cracked regions until the critical moisture threshold is reached, after which normal diffusion resumes. The CMM solves the coupled system of equations using the finite element method implemented in FEniCSx, with the workflow shown in Figure 2.

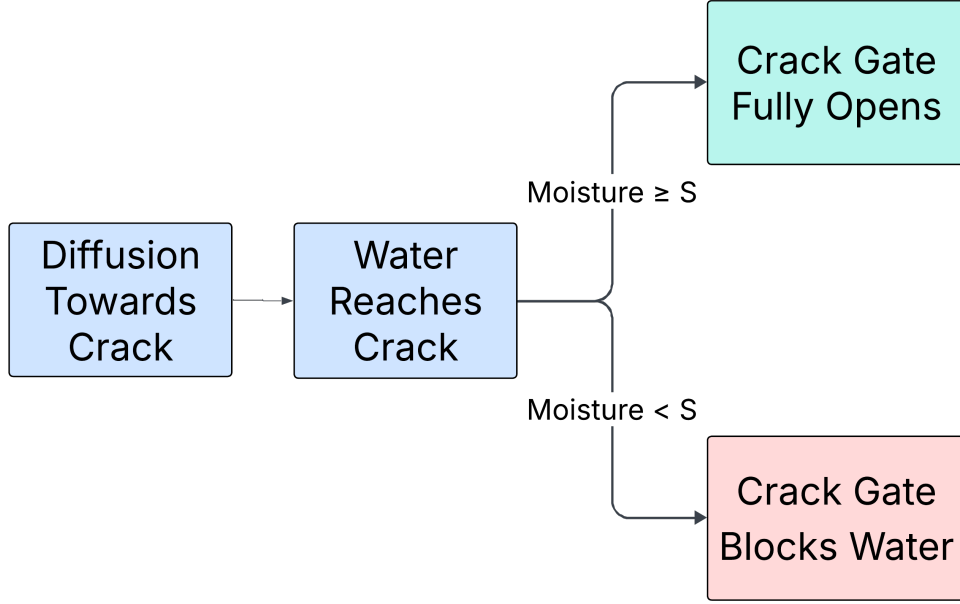


Fig. 2. Crack Membrane Model Logic Workflow

2.3 Machine Learning Model

Simulations in this study require solving millions of partial differential equations on fine element meshes, demanding substantial computational resources. Machine learning models trained on physics-based simulation data can learn underlying physical relationships and provide predictions 330 to 2,960,000 times faster than standalone finite element analysis [20].

Figure 3 shows a comparison of computational requirements between physics-based FEA and trained ML models. FEA requires multiple computational stages including mesh generation, PDE discretization, linear system assembly, iterative solution, and postprocessing, with the sparse linear system solver representing the most computationally intensive component. Conversely, ML inference requires only input data preprocessing and model evaluation, generating output predictions within milliseconds. However, it should be noted that ML model training requires substantial computational resources for training data generation through systematic FEA simulations and iterative parameter optimization via backpropagation.

The training of the ML models proceeded as follows. One million data points using various crack width indicator σ , cement availability γ , and time t values were used to generate H , the healing variable that is equal to 0 when not fully healed and 1 when fully healed. Five standard classification models were trained to learn the binary classification function $H(\sigma, \gamma, t)$. Namely, they

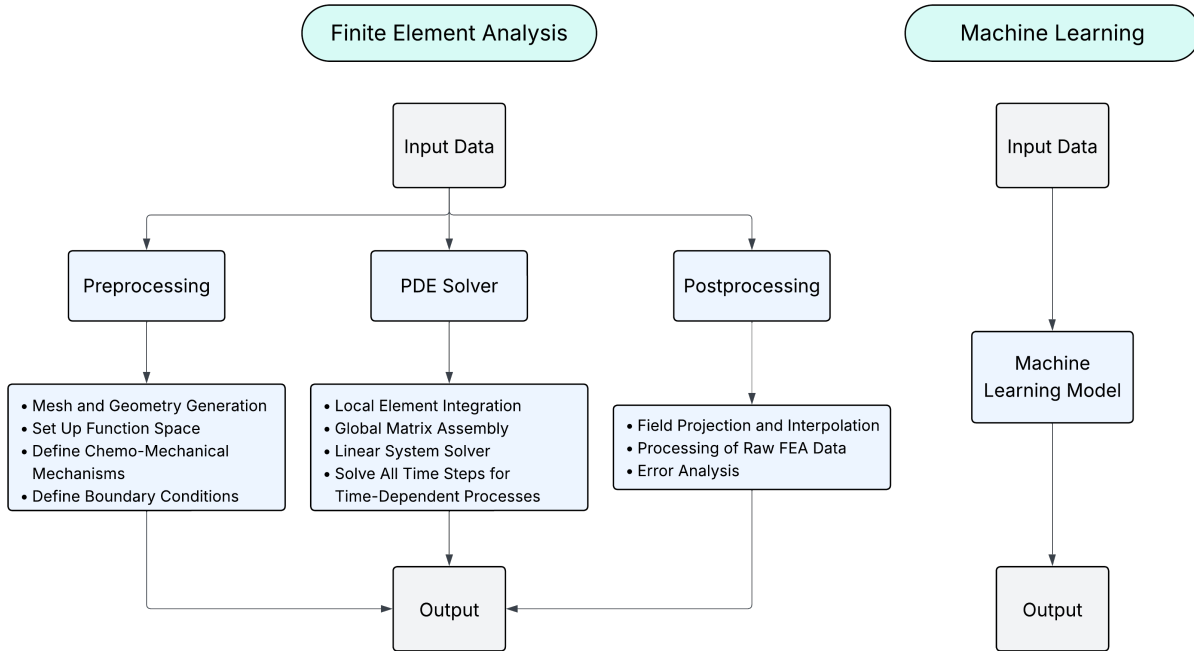


Fig. 3. Comparison of the Computing Complexities between Finite Element Analysis and Machine Learning

were the K-Nearest Neighbor (KNN), Logistic Regression, Naive Bayes, Support Vector Machine (SVM), and Neural Network Models. All of the models were trained out-of-the-box with the default parameters except for the neural network. Implementation utilized the TensorFlow and scikit-learn python libraries.

2.4 Simulation Cases and Preparation

This study used a 2D, 1×1 cm unit square mesh discretized into 2,048 triangles of equal size. The initial condition was a pre-defined line crack passing through the center of the domain and having incline angle β (Figure 4(a)). The impact of the crack angle on various properties and healing results was investigated. To initialize a continuous damage field, the baseline damage follows a Gaussian function as

$$d(x, y) = e^{-\frac{((x-0.5) \cos \beta - (y-0.5) \sin \beta)^2}{\sigma^2}} \quad (8)$$

where σ controls the width and smoothness of the Gaussian function. As an example, Figure 4(b) shows the initial damage field for the crack with parameter values $\beta = 0$ and $\sigma = \sqrt{0.0005} \approx 0.02236$ (99.7% of the crack spans about 0.0671 units, or 3σ).

To solve the diffusion equation, proper boundary conditions were prescribed. On the left side boundary, water supply was always available, i.e., the Dirichlet boundary condition of $U = 1$ was established. All other boundaries acted as completely sealed barriers with homogeneous Neumann conditions, where the normal gradient of U was set to zero.

In this work, the default numerical schemes in FEniCSx were used for the solution of the nonlinear diffusion equation. The Galerkin method with continuous Lagrange basis functions was used for the trial and test spaces, leading to a variational formulation of the diffusion operator that was assembled into sparse matrices. The temporal discretization was handled by the backward Euler

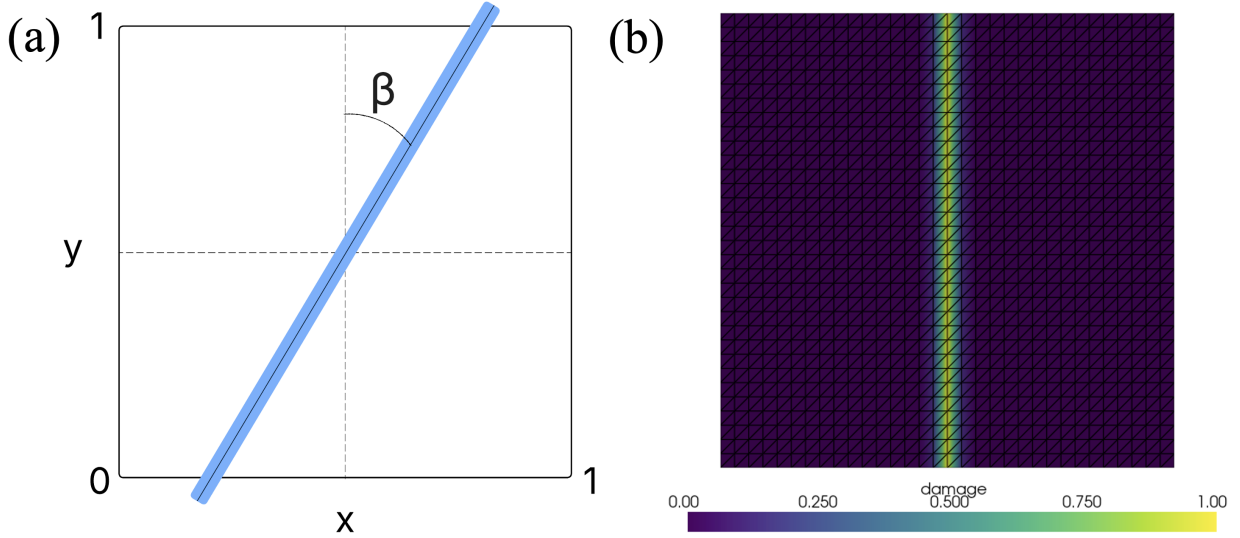


Fig. 4. Initial Condition for the Damage Field: (a) Definition of inclining angle β , (b) Example Scalar Damage Field During Pre-Cracking ($\beta = 0$, $\sigma^2 = 0.0005$)

(implicit Euler) scheme, which is first-order accurate, unconditionally stable, and widely used as the default choice for nonlinear parabolic PDEs.

One of the main goals of this study was to uncover the influence of physical parameters on relevant concrete recovery processes. Specifically, this study addressed the following three questions:

1. What is the influence of crack angle and crack width on healing time?
2. How do the healing progressions of CDM and CMM compare?
3. How accurately can machine learning be used to predict healing, while reducing computation time?

The models incorporate multiple interdependent parameters. Table 1 lists the primary parameters and material constants.

3 Results and Analysis

3.1 Healing Time vs. Crack Angle

The impact of the crack angle on the healing time was investigated using the CDM. As an example, Figure 5 shows the healing progress for $\beta = 45^\circ$ at four different representative moments in time. The healing time is defined as the time to heal 95% of the volume determined by the damage surface integral. Within the range of $\beta \in [0^\circ, 180^\circ]$, 37 values were chosen and simulated. Other parameters were kept constant. Specifically, their values were $\alpha = 0.01$, $\sigma = 0.0224$, and $\gamma = 0.0316$. The healing time versus crack angle plot is shown in Figure 6.

The model simulation provided important physical insights. Between $\beta = 0^\circ$ and 45° , the scatterplot exhibited a convex function with positive slope. As β increased within this range, water required greater diffusion distance to reach the rightmost crack endpoint, which approached the right boundary of the unit square. Due to symmetry about $\beta = 90^\circ$ in the range $\beta = [0^\circ, 180^\circ]$, this behavior was mirrored in the region from $\beta = 135^\circ$ to 180° . The middle region displayed different

Table 1. Model Parameters and Constants

Variable	Description	Constant or Parameter
D_{intact}	Diffusivity of water in pure, healed concrete	Constant: $10^{-8} \frac{\text{cm}^2}{\text{s}}$
D_{cracked}	Diffusivity of water in crack space, representing microcrack bridging, capillary bridges, partially healed CSH gel phases, and tortuous percolation	Constant: $10^{-7} \frac{\text{cm}^2}{\text{s}}$ (except for the analysis of crack width on healing time)
α	Healing rate constant of proportionality	Parameter
β	Angle of crack	Parameter
σ	Crack width indicator	Parameter
γ	Cement availability smoothing parameter	Parameter
p, q	Sharpness variables for diffusivity and cement availability, respectively	Constant; both set to 1

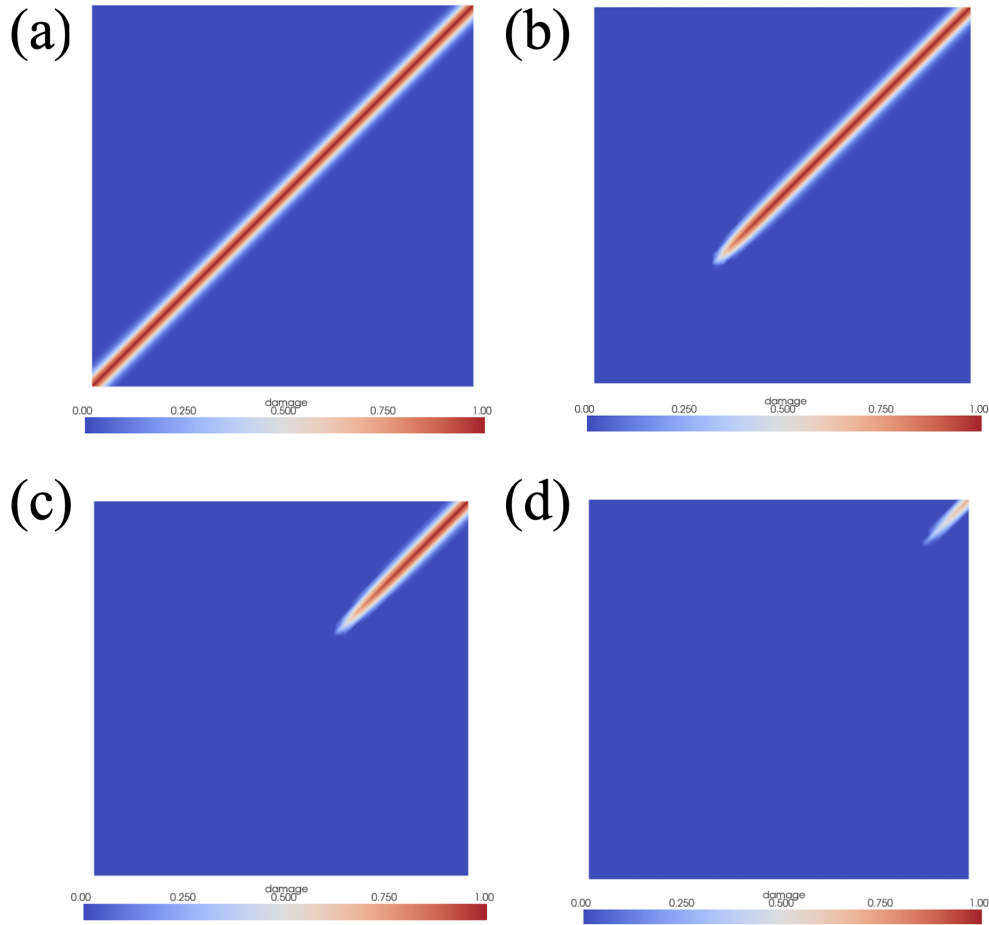


Fig. 5. Healing Progress for $\beta = 45^\circ$ at four different representative times. (a) Beginning of the simulation, (b) $\sim 1/3$ of the simulation time, (c) $\sim 2/3$ of the simulation time, (d) Final time.

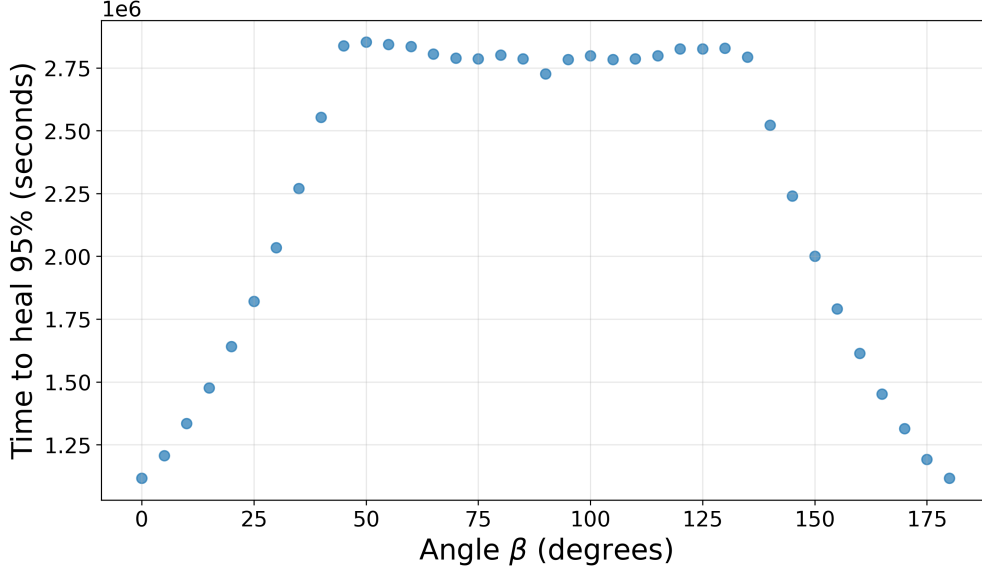


Fig. 6. Time to Heal 95% (seconds) vs. Crack Angle β (degrees)

healing behavior, where healing times remained relatively constant because the rightmost point maintained the same distance from the initial moisture source (1 cm), requiring water to travel identical distances for $\beta = 45^\circ$ to 135° . As β approached 90° (horizontal), healing time decreased slightly. Since the diffusion coefficient of cracked regions D_{cracked} exceeded that of intact concrete D_{intact} , water transport through cracks was faster than water transport through concrete. Crack length varied with orientation angle β , resulting in minimum healing time at $\beta = 90^\circ$ (shortest horizontal crack) and maximum healing times at $\beta = 45^\circ$ and 135° (longest diagonal cracks). Ultimately, diffusion distance was the primary factor determining the total healing time.

To examine the complexity of healing behavior across different crack angles β , healing progression plots were generated for $\beta = 0, \frac{\pi}{8}, \frac{\pi}{4},$ and $\frac{\pi}{2}$, as shown in Figure 7. Comparison between $\beta = 0$ and $\beta = \frac{\pi}{8}$ reveals that the crack at angle $\beta = \frac{\pi}{8}$ initiated healing earlier than the vertical crack ($\beta = 0$), as water reached the leftmost crack region sooner for $\beta = \frac{\pi}{8}$. However, the healing rate remained relatively slow because water had to continue saturating the domain until reaching the rightmost crack region of $\beta = \frac{\pi}{8}$. In contrast, once the vertical crack ($\beta = 0$) began healing, it healed at a significantly faster rate because water could immediately begin traversing the entire crack width. Consequently, the vertical crack achieved complete healing in a shorter time due to reduced diffusion distance. For $\beta = 0$ and $\frac{\pi}{8}$, the healing exhibited a symmetrical sigmoid shape. Comparison between the $\beta = \frac{\pi}{4}$ and $\beta = \frac{\pi}{2}$ cracks indicates that the horizontal crack ($\beta = \frac{\pi}{2}$) healed slightly faster than the $\beta = \frac{\pi}{4}$ crack. This observation is consistent with the Healing Time vs. Crack Angle plot in Figure 6, which demonstrates the influence of crack length on healing time when the crack mouth is in direct contact with the water source. Examination of the $\beta = \frac{\pi}{4}$ and $\frac{\pi}{2}$ graphs reveals rapid damage recovery at the beginning, then steadily increasing healing progress in the middle, and finally slowed healing progression as total healing approached 100%. Therefore, the 95% healed damage threshold was necessary; otherwise, healing times for full damage recovery would have been substantially longer, distorting the results. All graphs showed a 50% healing threshold at approximately 8×10^5 seconds, representing the time required for water to reach the crack center. This observation further supports the conclusion that primarily diffusion determined healing time.

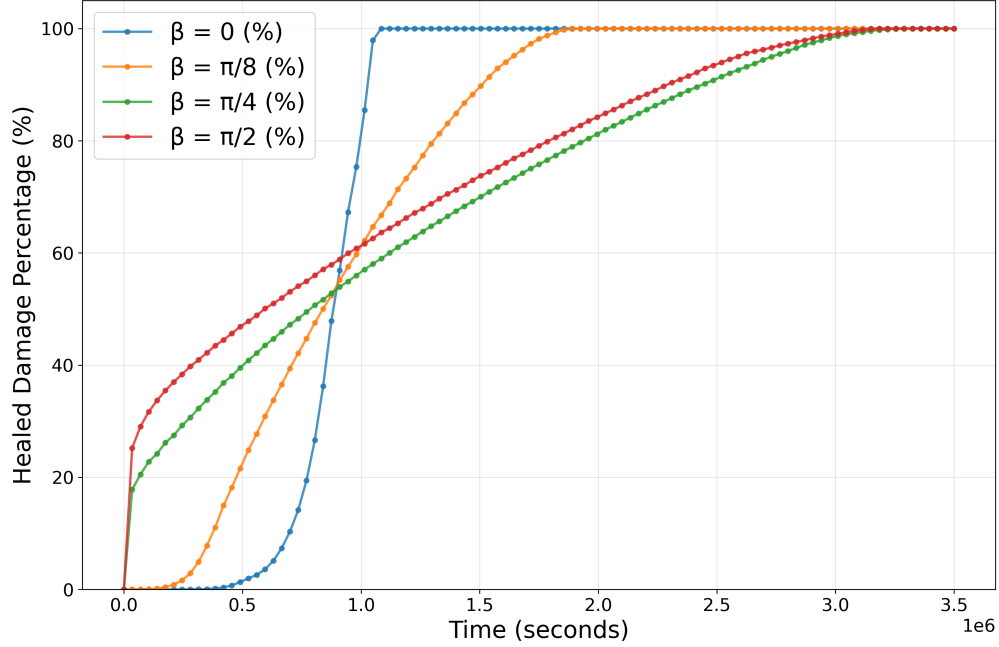


Fig. 7. Comparison of Healing Progress for Selected Crack Angles

3.2 Healing Time vs. Crack Width

The impact of the crack width on the healing time was investigated using the CDM. Two simulations were conducted with different parameter values. Within the range of $\sigma \in [0.005, 0.040]$ cm, 37 values were chosen and simulated. For Simulation 1, its parameter values were $D_{\text{intact}} = 10^{-8}$, $D_{\text{cracked}} = 10^{-9}$, $\alpha = 0.01$, $\beta = 0$, and $\gamma = 0.0316$. For Simulation 2, its parameter values were $D_{\text{intact}} = 10^{-8}$, $D_{\text{cracked}} = 10^{-7}$, $\alpha = 0.01$, $\beta = 0$, and $\gamma = 0.0316$. The healing time versus crack width plots are shown in Figure 8.

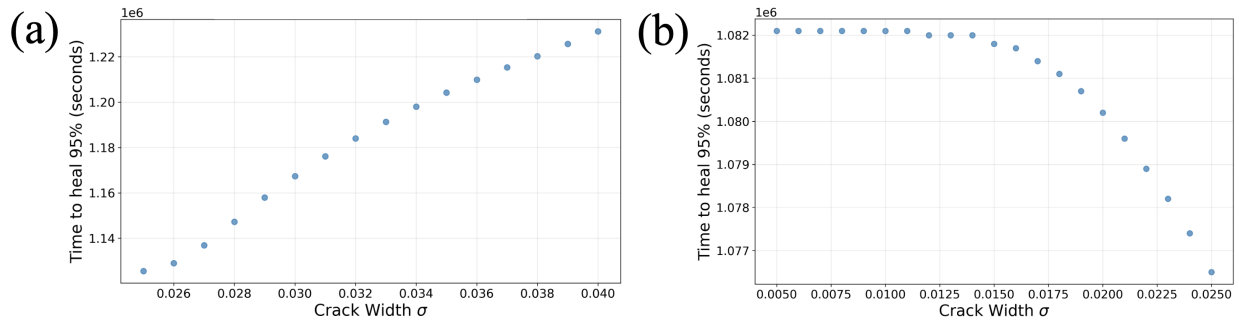


Fig. 8. Time to Heal 95% vs. Crack Width Parameter σ (cm): (a) Simulation 1, (b) Simulation 2

Simulation 1 exhibited a steadily increasing healing time as crack width increased from $\sigma = 0.025$ cm to $\sigma = 0.040$ cm, with slight concavity. By contrast, Simulation 2 revealed a decreasing concave relationship between healing time and crack width on the interval $\sigma = 0.005$ cm to $\sigma = 0.025$ cm. In Simulation 1, the diffusion coefficient in cracked regions was less than that in intact regions, resulting in increased healing time as crack width increased. In Simulation 2, the diffusion coefficient in cracked regions exceeded that in intact regions, enabling rapid diffusion and healing processes across

the crack interface. Since the healing process is diffusion-limited, larger crack widths reduce the effective diffusion distance, thereby decreasing the time required for water transport and allowing accelerated healing. The healing time increases with crack width when crack diffusivity is less than concrete diffusivity, whereas healing time decreases with increasing crack width when crack diffusivity exceeds concrete diffusivity.

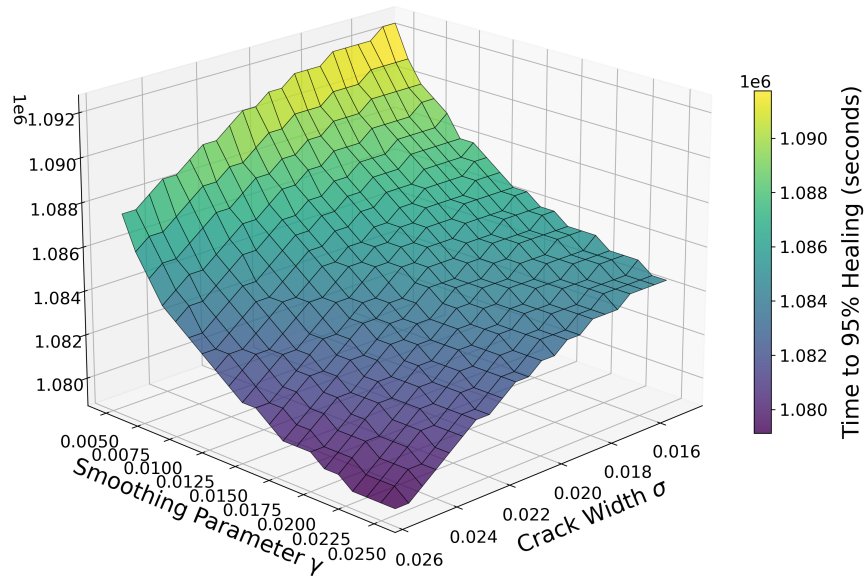


Fig. 9. 3D Plot of Healing Time, Crack Width, and Smoothing Parameter

The smoothing parameter γ is closely related to the crack width indicator σ and governs the spatial extent over which cement clinker can be transported and solidified. The healing time exhibits a functional dependence on both σ and γ when other parameters remain constant. Figure 9 presents this functional relationship as a three-dimensional surface plot. The analysis reveals that healing time increases as the smoothing parameter γ decreases. This relationship occurs because decreasing γ reduces the effective distance over which cement hydration can occur from its source. The healing time demonstrates a decreasing convex relationship with the smoothing parameter, indicating diminishing effects from increasing γ . Conversely, the healing time exhibits a decreasing concave relationship with crack width, displaying accelerated time effects as crack width increases. The functional shapes of σ and γ remain relatively stable when one parameter is varied while the other is held constant.

3.3 Healing Percentage vs. Time

The healing process is also of interest for practical use. Figure 10 illustrates the typical healing progression over time simulated using the CDM with parameter values $\alpha = 0.01$, $\beta = 0$, $\sigma = 0.0224$,

and $\gamma = 0.0316$. The healing process demonstrated an initial slow phase followed by acceleration as water saturated the entire crack. The healing rate approached an asymptotic maximum until complete crack healing was achieved. This behavior reflects the rate-limiting nature of water diffusion in the healing process. As damage decreased, water diffusion efficiency increased, resulting in higher healing rates. Similar healing patterns were observed across all parameter configurations with the CDM.

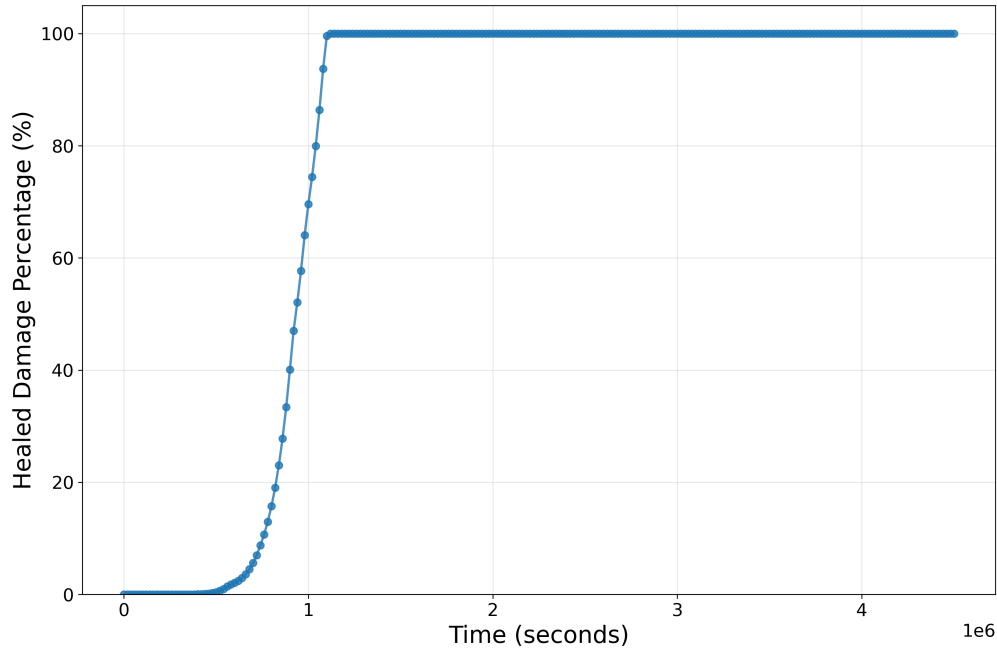


Fig. 10. Healing Percentage (%) as a Function of Time (seconds)

3.4 Comparison between CDM and CMM

The healing progressions of the two models, CDM and CMM, were contrasted, with parameter values set to $\alpha = 0.01$, $\beta = 0$, $\sigma = 0.0224$, and $\gamma = 0.0316$. The results are presented in Figure 11.

The analysis revealed a unique healing process with the CMM. There are three distinctive stages. Stage 1 represents the preliminary healing of partially damaged regions as water diffuses into these areas. Once water reaches the crack, it is stopped at the interface to prevent further movement. This is represented as the end of Stage 1 and a sharp corner in the graph. When further rightward water movement is suspended, Stage 2 of the healing process returns to the rate characteristic of healing within the already saturated regions. The end of Stage 2 occurs when the moisture threshold is reached, and the membrane begins releasing the water held at the left side of the crack boundary. Then, it enters the final phase, Stage 3, when water rapidly saturates the rest of the crack and heals the remainder. In Stage 3, the healing rate reaches a maximum. While the corners of this graph are quite dramatic, they have been emphasized through the crack gate sharpness parameter for the purposes of this illustration. To demonstrate these mechanisms, Figure 12 shows the saturation field progression of the Crack Membrane Model.

Comparing the two models in Figure 11, the added functionality of halting water movement until sufficient moisture is met in the Crack Membrane Model significantly lengthens the healing time. In the beginning (during Stage 1), the Crack Membrane Model exhibits a substantially slower

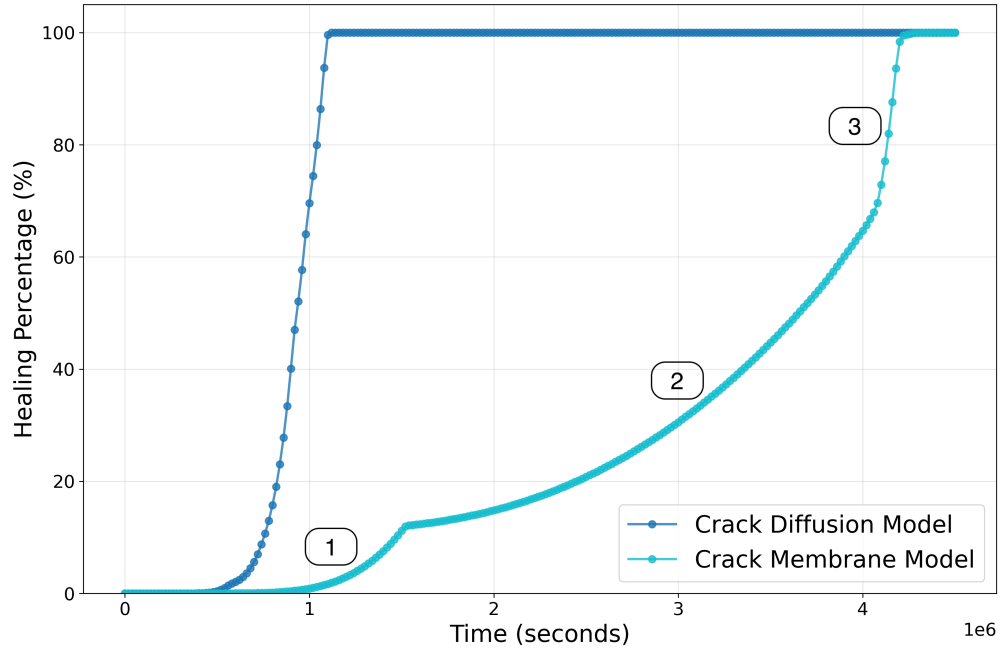


Fig. 11. Crack Diffusion vs. Crack Membrane Model Healing Percentage (%) as a Function of Time (seconds)

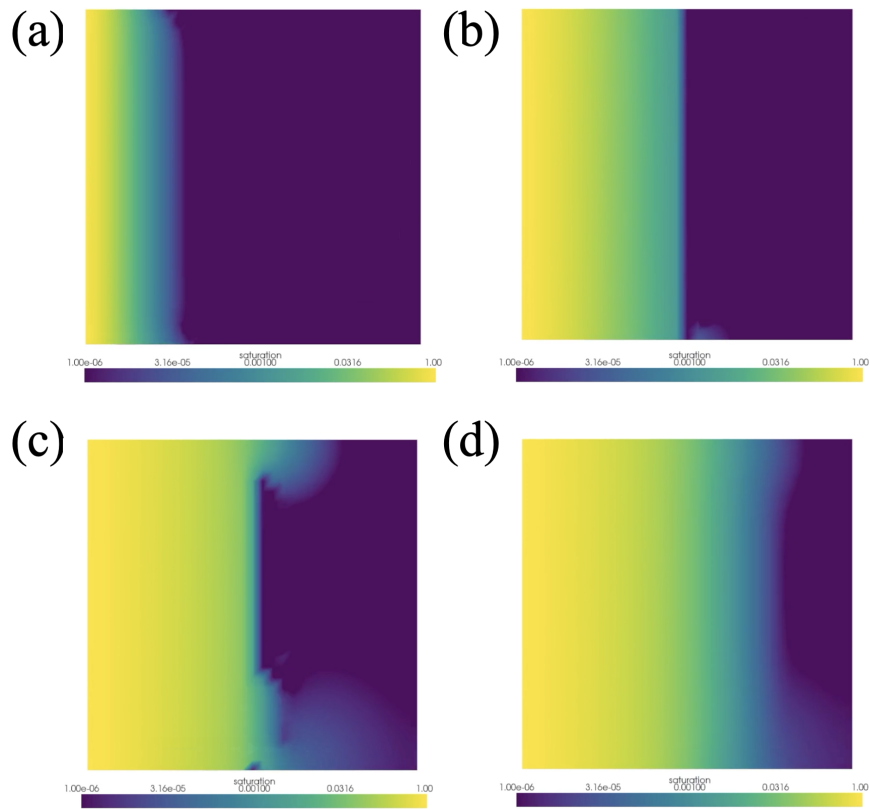


Fig. 12. Saturation Field of the Crack Membrane Model at four different representative times. (a) Diffusion toward the crack, (b) Water flow blocked at the crack membrane, (c) Partial water release, (d) Full water release.

initial healing rate compared to the Crack Diffusion Model. During Stage 3, the Crack Membrane Model achieves healing rates comparable to the final healing rates of the Crack Diffusion Model. The Crack Membrane Model provides a more accurate representation of the underlying physical and chemical processes. Experimental validation should demonstrate these characteristic transitions and distinct healing stages. However, the Crack Membrane Model’s additional calibration requirements increase analytical complexity. Thus, the Crack Diffusion Model was chosen as the primary model for the other analyses.

3.5 Performance Comparison of Machine Learning Models

The machine learning models were trained to predict the binary healing success H (0/1) based on the crack width σ , cement availability smoothing parameter γ , and time t . A dataset of 1,000,000 simulation samples was generated from the CDM using parameter ranges detailed in Table 2. Other parameters were kept constant. Specifically, their values were $\alpha = 0.01$, $\beta = \frac{\pi}{2}$, $\sigma = 0.0224$, and $\gamma = 0.0316$. The dataset was partitioned into training (60%), validation (20%), and test (20%) subsets for model development and evaluation. Performance metrics including accuracy, precision, recall, and f1-score [21] were computed on the test subset. The performance comparison is shown in Table 3 and Figure 13.

Table 2. Parameter Value Ranges and Sampling Units for ML Training Data Generation

Parameter	Lower Bound	Upper Bound	Step Size	Number of Steps
σ	0.001 cm	0.1 cm	0.001 cm	100
γ	0.001 cm	0.1 cm	0.001 cm	100
t	30,000 s	3,000,000 s	30,000 s	100

Table 3. Machine Learning Model Performance Comparison

Metric	KNN	Naive Bayes	Logistic Regression	SVM	Neural Network
Accuracy	0.9971	0.9481	0.9879	0.9936	0.9980
Precision	0.9972	0.9618	0.9886	0.9939	0.9980
Recall	0.9971	0.9481	0.9879	0.9936	0.9980
F1-Score	0.9972	0.9513	0.9881	0.9937	0.9980

The neural network achieved the highest performance across all metrics (accuracy=0.9980, precision=0.9980, recall=0.9980, f1-score=0.9980) using a 3-32-32-1 architecture with ReLU activation, dropout=0.2, learning rate=0.001, batch size=32, and 100 epochs. The performances of KNN, SVM, Logistic Regression, and Naive Bayes followed, in that order. It should be noted that the neural network took the longest time to train, while the KNN algorithm was almost instantaneous. Thus, for maximal performance, the neural network is the best pick. For a combination of performance and training time, KNN is the best pick.

3.6 Limitations and Future Improvements

Several limitations constrain the current model’s applicability. First, model parameters were estimated rather than experimentally calibrated, potentially affecting quantitative predictions while

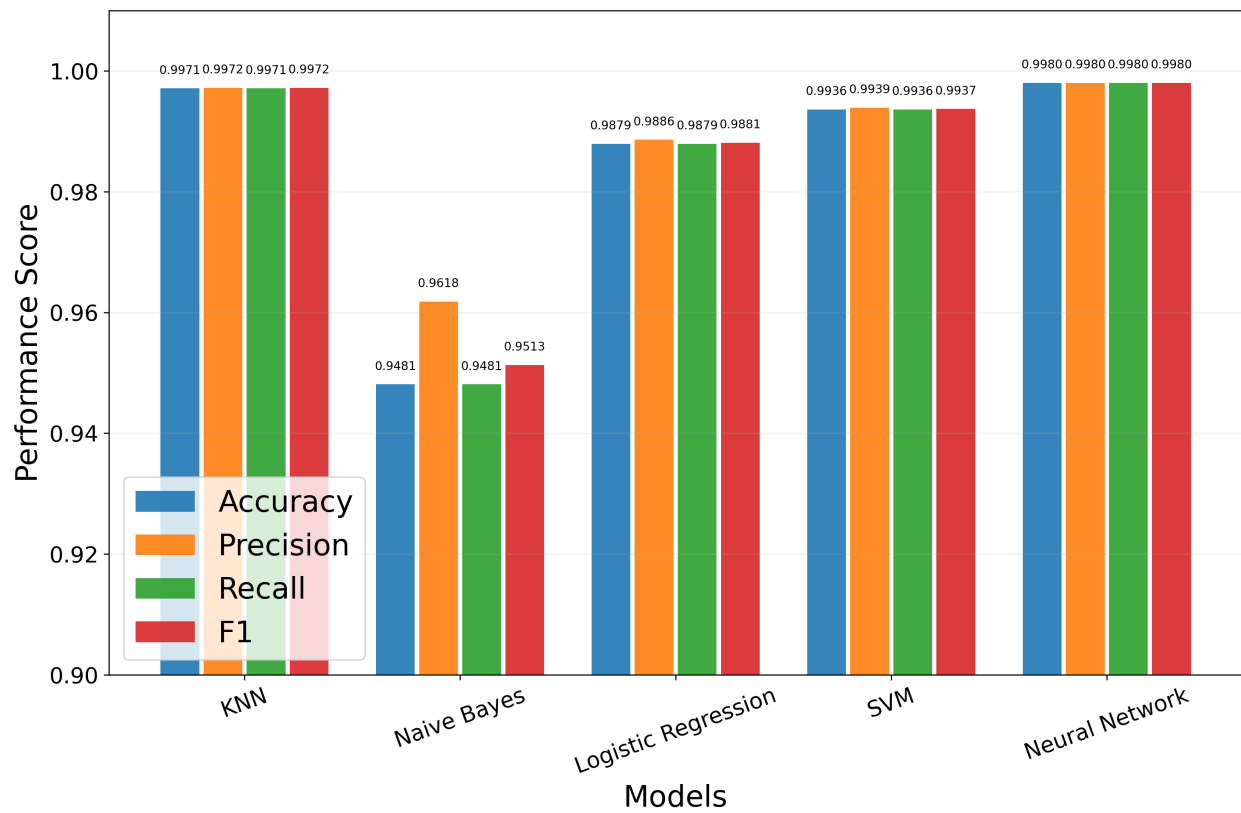


Fig. 13. Machine Learning Model Performance Comparison Bar Chart (accuracy, precision, recall, f1-score)

preserving qualitative trends. Second, crack geometries were simplified to Gaussian distributions, whereas real cracks exhibit complex propagation patterns that could be better captured through techniques such as X-ray microtomography. Third, the model assumes constant cement availability in newly healed regions, which may overestimate long-term healing capacity. Fourth, water transport is modeled through diffusion rather than pressure-driven flow governed by porous media laws such as Darcy’s law.

Future work should address these limitations through experimental validation, realistic crack geometry implementation, and incorporation of porous media flow mechanics. Additionally, the model could be extended to three-dimensional domains to capture volumetric healing effects, cyclic loading scenarios to assess long-term durability, and strength recovery calculations through post-processing of damage fields. These extensions would enhance the model’s predictive capability for real-world applications. The ML models can be further analyzed using explainable AI (XAI) to provide insights into the model’s predictions.

4 Conclusions

This study developed two coupled finite element models for simulating autogenous self-healing concrete behavior, addressing the critical need for computational tools to evaluate this promising technology for infrastructure reinforcement and sustainability. The Crack Diffusion Model (CDM) and Crack Membrane Model (CMM) successfully integrated time-dependent feedback mechanisms, logarithmic interpolation of diffusion coefficients, and damage evolution based on cement and water availability. CMM adds a binary gate mechanism to the CDM to simulate the moisture threshold buildup and rapid healing after gate activation.

The models revealed several key insights into healing behavior. Crack orientation significantly influences healing time, with diffusion distance to crack endpoints being the dominant factor rather than crack length. Healing time increases from 0° to 45° as water travels farther to reach crack endpoints, then remains relatively constant from 45° to 135° due to similar diffusion distances, with a slight decrease at 90° due to shorter crack length. The relationship between crack width and healing time depends on the relative diffusivities of cracked versus intact regions, demonstrating the importance of material parameter selection.

The CMM provides a more realistic representation of healing physics through its binary gate mechanism, showing three distinct healing phases: initial diffusion, moisture buildup, and rapid healing after gate activation. However, the CDM offers computational efficiency advantages for parametric studies.

Machine learning models trained on over one million simulation data points achieved high accuracy (up to 99.8% for neural networks) in predicting healing outcomes, demonstrating the potential for rapid screening of design parameters. The k-nearest neighbors algorithm provided an optimal balance between accuracy (99.7%) and computational efficiency.

These findings contribute to the understanding of autogenous healing mechanisms and provide a foundation for optimizing self-healing concrete formulations. The models address limitations in existing literature by incorporating time-dependent feedback, realistic cement availability smoothing, and machine learning integration for rapid prediction. While experimental validation remains necessary for quantitative accuracy, the models offer valuable insights for guiding future laboratory studies and field applications.

The computational framework developed in this study could accelerate the adoption of self-healing concrete technologies, potentially reducing the environmental and economic costs associated with infrastructure maintenance and repair. Future work should focus on experimental calibration,

three-dimensional extensions, and cyclic loading scenarios to further enhance predictive capability for real-world applications.

Acknowledgments

The author is grateful for the guidance and insights provided by Natalie Ronco from Cambridge University.

Data Availability

A permanent copy of code, data, and outputs of this work are publicly available at <https://github.com/william-liu0/concrete-healing-model>.

References

- [1] Manh-Thuong Nguyen, Carlos A. Fernandez, Md Mostofa Haider, Kung-Hui Chu, Guoqing Jian, Somayeh Nassiri, Difan Zhang, Roger Rousseau, and Vassiliki-Alexandra Glezakou. Toward Self-Healing Concrete Infrastructure: Review of Experiments and Simulations across Scales. *Chemical Reviews*, 123(18):10838–10876, September 2023.
- [2] Nick Gromicko and Kenton Shepard. The history of concrete. <https://www.nachi.org/history-of-concrete.htm>, 2025. Accessed 30 July 2025.
- [3] Jannik Linder. Concrete industry statistics: Market data report 2025. <https://gitnux.org/concrete-industry-statistics/>, 2025. Accessed 30 July 2025.
- [4] Robbie M. Andrew. Global CO2 emissions from cement production, May 2024.
- [5] Michael Purton. Cement production sustainable concrete co2 emissions. <https://www.weforum.org/stories/2024/09/cement-production-sustainable-concrete-co2-emissions/>, 2024. Accessed 30 July 2025.
- [6] Ben Skinner and Radhika Lalit. With concrete, less is more. <https://rmi.org/with-concrete-less-is-more/>, January 2023. Accessed 30 July 2025.
- [7] Paul Noyce and Gina Crevello. Durability of reinforced concrete. <https://www.structuremag.org/article/durability-of-reinforced-concrete/>, January 2016. Accessed 30 July 2025.
- [8] American Society of Civil Engineers. Asce’s 2025 infrastructure report card. <https://infrastructurereportcard.org/>, 2025. Accessed 30 July 2025.
- [9] NACE International. Global cost of corrosion. <http://impact.nace.org/economic-impact.aspx>, 2025. Accessed 30 July 2025.
- [10] Nataliya Hearn. Self-sealing, autogenous healing and continued hydration: What is the difference? *Materials and Structures*, 31(8):563–567, October 1998.
- [11] Carola Edvardsen. Water Permeability and Autogenous Healing of Cracks in Concrete. *Materials Journal*, 96(4):448–454, July 1999.

- [12] Mugahed Amran, Ali M Onaizi, Roman Fediuk, Nikolai Ivanovicn Vatin, Raizal Saifulnaz Muhammad Rashid, Hakim Abdelgader, and Togay Ozbakkaloglu. Self-healing concrete as a prospective construction material: A review. *Materials*, 15(9):3214, April 2022.
- [13] USC Viterbi School of Engineering. Can concrete heal its own cracks without losing its strength? <https://viterbischool.usc.edu/news/2022/03/can-concrete-heal-its-own-cracks-without-losing-its-strength/>, 2022. Accessed 30 July 2025.
- [14] BBC. 'self-healing' concrete trial launched in south wales. <https://www.bbc.com/news/uk-wales-south-east-wales-34658038>, 2015. Accessed 30 July 2025.
- [15] B. Hilloulin, F. Grondin, M. Matallah, and A. Loukili. Modelling of autogenous healing in ultra high performance concrete. *Cement and Concrete Research*, 61–62:64–70, July 2014.
- [16] Ajitanshu Vedrtnam, Kishor Kalauni, and M. T. Palou. Finite element simulation of bacterial self-healing in concrete using microstructural transport and precipitation modeling. *Scientific Reports*, 15:15809, May 2025.
- [17] H Shahsavari, M Baghani, S Sohrabpour, and R Naghdabadi. Continuum damage-healing constitutive modeling for concrete materials through stress spectral decomposition. *International Journal of Damage Mechanics*, 25(6):900–918, August 2016.
- [18] Qing Chen, Xiangyong Liu, Hehua Zhu, J Woody Ju, Xie Yongjian, Zhengwu Jiang, and Zhiguo Yan. Continuum damage-healing framework for the hydration induced self-healing of the cementitious composite. *International Journal of Damage Mechanics*, 30(5):681–699, May 2021.
- [19] FEniCS. <https://fenicsproject.org/>, 2025. Accessed 30 July 2025.
- [20] Rajat Nath, Sandeep Patil, and Amit Kumar. Machine learning accelerated finite element analysis. *Computational Mechanics*, 65(3):567–589, 2020.
- [21] Trevor Hastie, Robert Tibshirani, and Jerome Friedman. *The Elements of Statistical Learning: Data Mining, Inference, and Prediction*. Springer, New York, 2nd edition, 2009.